



1 **Linearization of the effect of slit function changes** 2 **for improving OMI ozone profile retrievals**

3 **Juseon Bak^{a,*}, Xiong Liu^a, Kang Sun^b, Kelly Chance^a, Jae-Hwan Kim^c**

4 ^a*Harvard-Smithsonian Center for Astrophysics, Cambridge, MA, USA*

5 ^b*Research and Education in eNergy, Environment and Water Institute, University at Buffalo, Buffalo, NY, USA*

6 ^c*Atmospheric Science Department, Pusan National University, Busan, Korea*

7 *Corresponding Author (juseon.bak@cfa.harvard.edu)

8 **Abstract**

9
10 We introduce a method that reduces the spectral fit residuals caused by the slit function errors in an
11 optimal estimation based spectral fitting process to improve ozone profile retrievals from the Ozone
12 Monitoring Instrument (OMI) ultraviolet measurements (270-330 nm). Previously, a slit function was
13 parameterized as a standard Gaussian by fitting the Full Width at Half Maximum (FWHM) of the slit
14 function from climatological OMI solar irradiances. This cannot account for the temporal variation of slit
15 function in irradiance, the intra-orbit slit function changes due to thermally-induced change and scene
16 inhomogeneity, and potential differences in the slit functions of irradiance and radiance measurements. As
17 a result, radiance simulation errors may be induced due to using the convolved reference spectra with
18 incorrect slit functions. To better represent the shape of the slit functions, we implement a more generic
19 super Gaussian slit function with two free parameters (slit width and shape factor); it becomes standard
20 Gaussian when the shape factor is fixed to be 2. The effects of errors in slit function parameters on radiance
21 spectra, referred as “Pseudo Absorbers (PAs)”, are linearized by convolving high-resolution cross sections
22 or simulated radiances with the partial derivatives of the slit function with respect to the slit parameters.
23 The PAs are included in the spectral fitting scaled by fitting coefficients that are iteratively adjusted as
24 elements of the state vector along with ozone and other fitting parameters. The fit coefficients vary with
25 cross-track and along-track pixels and show sensitivity to heterogeneous scenes. The total PA spectrum is
26 quite similar in the Hartley band below 310 nm for both standard and super Gaussians, but is more distinctly
27 structured in the Huggins band above 310 nm with the use of super Gaussian slit functions. Finally, we
28 demonstrate that some spikes of fitting residuals are slightly smoothed by accounting for the slit function



29 errors. Comparisons with ozonesondes demonstrate substantial improvements with the use of PAs for both
30 standard and super Gaussians, especially for reducing the systematic biases in the tropics and mid-latitudes
31 and reducing the standard deviations at high-latitudes. Including PAs also makes the retrievals consistent
32 between standard and super Gaussians. This study corroborates the slit function differences between
33 radiance and irradiance demonstrating that it is important to account for such differences in the ozone profile
34 retrievals.

35

36 **1. Introduction**

37 The fitting of the measured spectrum to the simulated spectrum is the most basic concept for the analysis
38 of the Earth's atmospheric constituents from satellite measurements. Therefore, the accurate calibration and
39 simulation of measurements are essential for the successful retrieval of atmospheric constituents. The
40 knowledge of the instrumental spectral response function (ISRF) or slit function could affect the accuracies
41 of both calibration and simulation, as it is required for the convolution of a high-resolution reference
42 spectrum onto instrument's spectral resolution in the wavelength calibration and for the convolution of
43 high-resolution absorption cross section spectra or simulated radiance spectrum in the calculation of
44 radiance at instrumental resolution. Compared to other trace gases, the retrieval of ozone profiles could be
45 more susceptible to the accuracy of ISRFs due to the large spectral range, where the radiance spans a few
46 orders of magnitude and to the fact that the spectral fingerprint for the tropospheric ozone is primarily
47 provided by narrow and weak absorption features of the temperature-dependent Huggins bands (320-360
48 nm). Therefore, the efforts of characterizing and verifying the ISRFs have preceded the analyses of ozone
49 profiles from the satellite/aircraft measurements (Liu et al., 2005, 2010; Cai et al., 2012; Liu et al., 2015;
50 Sun et al. 2017; Bak et al., 2017).

51 For space-borne instruments, ISRFs are typically characterized as a function of the detector dimensions
52 using a tunable laser source prior to the launch (Dirksen et al., 2006; Liu et al., 2015; van Hees et al., 2018).
53 However, the preflight measured ISRFs could be inconsistent with those after launch due to the orbital
54 movement and the instrument temperature change (Beirle et al., 2017; Sun et al., 2017). Therefore, the post-
55 launch ISRFs have been typically parameterized through a cross-correlation of the measured solar
56 irradiance to a high-resolution solar spectrum (Caspar and Chance, 1997), assuming Gaussian-like shapes.
57 The direct retrieval of the ISRFs from radiances has not typically been done due to the complication of
58 taking the atmospheric trace gas absorption and Ring effect into account in the cross-correlation procedure
59 and the slow-down of the fitting process. However, slit function differences between radiance and
60 irradiance could exist due to scene heterogeneity, differences in stray light between radiance and radiance,



61 intra-orbit instrumental changes, and the instrument temperature change (Beirle et al., 2017; Sun et al.,
62 2017). In addition, using temporally invariant slit functions derived from climatological solar spectra in the
63 retrievals could cause the long-term trend errors if instrument degradation occurs. Therefore, there is room
64 for improving our trace gas retrievals by accounting for the effects of the different ISRFs between radiance
65 and irradiance on the spectral fitting and on the pixel-to-pixel basis. The “Pseudo Absorber (PA)” is a
66 common concept in spectral fitting to account for the effect of the physical phenomena that is difficult or
67 computationally demanding to be simulated in the radiative transfer calculation, like spectral misalignments
68 (shift and stretch) between radiance and irradiance, Ring effect, spectral undersampling, and additive stray-
69 light offsets. The pseudo absorption spectrum can be derived from a finite-different scheme (e.g. Azam and
70 Richter, 2015) or a linearization scheme via a Taylor expansion (e.g. Beirle et al., 2013; 2017); the latter
71 approach is more efficient than the former one, but less accurate because only the first term of the Taylor
72 series is typically taken into account for simplicity. Beirle et al. (2013) introduced a linearization scheme
73 to account for spectral misalignments between radiance and irradiance and then included them as a pseudo-
74 absorber in DOAS-based NO₂ and BrO fittings. Similarly, Beirle et al. (2017) linearized the effect of the
75 change of the ISRF parameterized as a super Gaussian on GOME-2 solar irradiance spectra to characterize
76 the slit function change over time and wavelength. Sun et al. (2017) derived on-orbit slit functions from
77 solar irradiance spectra measured by the Ozone Monitoring Instrument (OMI) (Levelt et al., 2006) assuming
78 standard Gaussian, super Gaussian, and preflight ISRFs with adjusted widths. The derived on-orbit slit
79 functions, showing significant cross-track dependence that cannot be represented by preflight ISRFs,
80 substantially improve the retrievals by the Smithsonian Astrophysical Observatory (SAO) ozone profile
81 algorithm. However, it is not fully understood why the use of super Gaussian or stretched preflight functions,
82 which are supposed to better model the OMI spectra as indicated by smaller mean fitting residuals, does
83 not improve the retrievals over the use of standard Gaussian especially in the standard deviations of the
84 differences with relative to ozonesonde observations. This study suggested that the slit functions derived
85 from solar spectra might not fully represent those in radiance spectra.

86 As such, the objective of this paper is to implement the slit function linearization proposed by Beirle
87 et al. (2017) into the optimal estimation based spectral fitting of the SAO ozone profile algorithm. We
88 further improve the slit function parameterization by accounting for the differences between radiance and
89 irradiance slit functions on a pixel-by-pixel basis, and ultimately to improve OMI ozone profile retrievals.
90 This paper is organized as follows: after a mathematical description of the linearization of slit function
91 changes using the generic super Gaussian function, we introduce how to apply them practically in an
92 optimal estimation based spectral fit procedure (Section 2). This linearization scheme is differently
93 implemented, depending on the simulation scheme of measured spectra using high resolution radiances or
94 effective cross section data, respectively. Section 3 characterizes the derived pseudo absorber spectra, along



95 with the evaluations of ozone profile retrievals using independent ozonesonde observations as a reference
 96 dataset. Finally, the summary of this study is given in Section 4.

97 2. Method

98 2.1 Super Gaussian linearization

99 The slit function parameterization and linearization are briefly summarized from Beirle et al. (2017),
 100 focusing on what we need to derive the pseudo absorbers in the terms of the optimal estimation based fitting
 101 process. The slit function can be parameterized with the slit width w , and shape factor k assuming the
 102 super Gaussian, S as:

$$103 \quad S(\Delta\lambda) = A(w, k) \times \exp\left[-\left|\frac{\Delta\lambda}{w}\right|^k\right], \quad (1)$$

104 where $A(w, k)$ is $\frac{k}{2\sigma_g \Gamma(\frac{1}{k})}$ with Γ representing the gamma function. This equation allows many forms of
 105 distributions by varying k : the top-peaked function ($k < 2$), the standard Gaussian function ($k = 2$), and the
 106 flat-topped function ($k > 2$). w is converted to the Full Width at Half Maximum (FWHM) via the relationship
 107 of $\text{FWHM} = 2^{\frac{1}{k}} \sqrt{\ln 2} w$. We investigate the impact of including one more slit parameter k on the OMI ISRF
 108 fit results over the standard Gaussian using OMI daily solar measurements. As an example, time-series
 109 (2005-2015) of the fitted slit width and shape factor in 310-330 nm are displayed in Figure 1.a. The FWHM
 110 and shape factor of the super Gaussian function is on average 0.44 nm and 2.9, respectively, while the
 111 FWHM of the standard Gaussian is 0.395 nm. The degradation of the OMI slit functions became relatively
 112 visible after 2011. The high wavelength stability (0.003 nm) is seen in Figure 1b, verifying that better
 113 calibration stability is performed with super Gaussian slit functions as abnormal deviations of wavelength
 114 shifts are derived with standard Gaussian slit functions.

115 The effect of changing the slit parameters p on the slit function can be linearized by the first-order
 116 Taylor expansion approximation around $S_o = S(p_o)$:

$$117 \quad \Delta S = S - S_o \approx \Delta p \frac{\partial S}{\partial p}, \quad (2)$$

118 and thus the effect of changes of S on the convolved high-resolution spectrum can be parameterized as

$$119 \quad \Delta I = I - I_o = S \otimes I_h - S_o \otimes I_h = \Delta S \otimes I_h, \quad (3)$$

120 where the convolved spectrum is $I = S \otimes I_h$. Consequently, the partial derivatives of I with respect to slit
 121 parameters, p are defined as



122
$$\frac{\partial I}{\partial p} = \frac{\partial S}{\partial p} \otimes I_h. \quad (4)$$

123 In Beierle et al. (2017), $\frac{\partial I}{\partial p}$ refers to J_p as “resolution correction spectra (RCS)”. In Figure 2, we present
124 an example of J_p over the typical ozone profile fit range (270-330 nm) through the convolution of high-
125 resolution ozone cross sections (δ_h) with the derivatives of the super Gaussian ($\frac{\partial S}{\partial p}$). The baseline S_0 is
126 defined with $w=0.26$ nm and $k=2.6$, which are averaged parameters from climatological OMI solar
127 irradiance spectra in the UV2 band (310-330 nm). Note that this w value corresponds to a FWHM of 0.45
128 nm. The change of the assumed OMI slit function causes a highly structured spectral response over the
129 whole fitting window. However, the relative magnitude of the responses with respect to both slit parameters
130 is more distinct in the Huggins band (>310 nm) where narrow absorption features are observed as shown
131 in Figure 2.a. An anti-correlation (-0.92) is found between $\frac{\partial \ln \delta}{\partial w}$ and $\frac{\partial \ln \delta}{\partial k}$ while the response of the unit
132 change of the slit width to the convolved spectrum is dominant against that of the shape factor.

133

134 **2.2 Implementation of the slit function linearization in the SAO ozone profile algorithm**

135

136 We implement the slit function linearization in the SAO ozone profile algorithm (Liu et al. 2010), which
137 is routinely being performed to produce the OMI PROFOZ product
138 (<https://avdc.gsfc.nasa.gov/index.php?site=1389025893&id=74>). Two spectral windows (i.e., 270-309 nm
139 in the UV1 band and 312-330 nm in the UV2 band) are employed to retrieve ozone profiles from OMI BU
140 measurements. To match the different spatial resolutions between UV1 and UV2 bands, every two cross-
141 track pixels are averaged for UV2 band, resulting into 30 positions with the spatial resolution of 48 km
142 (across-track) \times 13 km (along-track) at nadir position. The non-linear optimal estimation based fitting is
143 iterated toward minimizing the fitting residuals between measured and simulated radiances and
144 simultaneously between a priori and estimated ozone values. A priori ozone information is taken from a
145 tropopause-based (TB) ozone profile climatology (Bak et al., 2013). The Vector Linearized Discrete
146 Ordinate Radiative Transfer model (VLIDORT) (Spurr, 2008) is used to simulate the radiances and their
147 derivatives with respect to geophysical parameters. The radiance calculation is made for the Rayleigh
148 atmosphere, where the incoming sunlight is simply absorbed by ozone and other trace gases, scattered by
149 air molecules, and reflected by surfaces/clouds assumed as a Lambertian surface. Besides these physical
150 phenomena, the others are treated as PAs to the spectral response such as Ring effect, additive offset, and
151 spectral shifts due to misalignments of radiance relative to irradiance and ozone cross sections. In the SAO
152 algorithm, these PAs are derived using the finite differences of the radiances with and without perturbation



153 to a phenomenon, except for the Ring spectrum that is calculated using a first-order single scattering
154 rotational Raman scattering model (Sioris and Evans, 2000).

155 In this paper, we introduce new PAs to account for the radiance simulation errors caused by the slit
156 function errors. The OMI ISRFs have been parameterized as a standard Gaussian from climatological OMI
157 solar irradiances for each UV1 and UV2 band and thereby these PAs could take into account the spectral
158 fitting responses caused by temporal variations of the slit function. This ozone fitting procedure uses ISRFs
159 to convolve high resolution absorption spectra, taken from Brion et al. (1993) for ozone absorption cross
160 section and Wilmouth et al. (1999) for BrO absorption cross section. Our algorithm has implemented two
161 different convolution processes, i.e. the effective cross section approach in Liu et al (2010) and the high-
162 resolution convolution approach described in Kim et al. (2013), respectively and thereby this paper also
163 introduces how to derive the derivatives of the OMI radiances with respect to ISRF changes in these two
164 approaches. Although the latter is the current approach, we also implement and present the linearization
165 with the first approach, which is typically used for other trace gas retrieval algorithms.

166 In Liu et al (2010), VLIDORT simulates the radiances at OMI spectral grids (λ_{omi}) using effective cross
167 sections that are produced by convolving high-resolution cross sections with the OMI ISRF. Therefore, we
168 apply a similar convolution process of matching the high-resolution cross section spectrum with OMI
169 spectrum to derive the partial derivative of σ_x with respect to slit parameter, p as follows:

170
$$\frac{\partial \sigma_x}{\partial p} = \frac{\partial S}{\partial p} \otimes \sigma_{x,h}, \quad (5)$$

171 where $\sigma_{x,h}$ is a high-resolution absorption spectrum for ozone and BrO, respectively. Due to the dominant
172 ozone absorption over the BrO absorption, the derivative of BrO cross section with respect to p is neglected
173 here. This partial derivative of ozone is then converted to the partial derivative of radiance through the chain
174 rule with the analytical ozone weighting function ($\frac{d \ln I}{d O_3}$), calculated from VLIDORT, as follows:

175
$$\frac{\partial \ln I}{\partial p} = \frac{\partial \ln I}{\partial O_3} \frac{\partial \sigma}{\partial p} \frac{O_3}{\sigma}. \quad (6)$$

177 This simulation process is hereafter referred to as “effective resolution cross section (ER) simulation”.

178 As described in Kim et al. (2013), the radiative transfer calculation in the SAO ozone profile algorithm
179 has been performed using high-resolution extinction spectra at the optimized sampling intervals for
180 resolving the ozone absorption features, which are a 1.0 nm below 300 nm and 0.4 nm above 300 nm. These
181 sampling intervals are coarser than actual OMI sampling grids with approximately half the number of
182 wavelengths. The coarser sampled simulated radiances are then interpolated to a fine grid of 0.05 nm
183 assisted by the weighting functions with respect to absorption and Rayleigh optical depth:



$$I(\lambda_h) = I(\lambda_c) + \frac{\partial I(\lambda_c)}{\partial \Delta_l^{gas}} \left(\Delta_l^{gas}(\lambda_h) - \Delta_l^{gas}(\lambda_c) \right) + \frac{\partial I(\lambda_c)}{\partial \Delta_l^{ray}} \left(\Delta_l^{ray}(\lambda_h) - \Delta_l^{ray}(\lambda_c) \right), \quad (7)$$

where Δ_l^{gas} and Δ_l^{ray} are the optical thickness (the product of cross section and layer column density) at each layer for trace gas absorption and Rayleigh scattering, respectively. The convolution is then applied to these simulated high-resolution radiances, $I(\lambda_h)$ with assumed slit functions and derivatives, respectively, and thereby $I(\lambda_{omi})$ and $\frac{\partial \ln I}{\partial p}$ is calculated. This simulation process is hereafter referred to as “high-resolution cross section (HR) simulation”. The ER simulation is more commonly implemented in the trace gas retrievals in the UV and visible, but the HR simulation allows for more accurate fitting residuals to, better than 0.1 % (Kim et al., 2013) as well as shorter computation time. $\frac{\partial \ln I}{\partial p}$ is scaled by the fitting coefficients, Δp , to account for the actual size of the spectral structures caused by the slit function differences between radiance and irradiance spectra. The total “pseudo absorber (PA)” for the Super Gaussian slit function linearization is expressed as:

$$PA = \frac{\partial \ln I}{\partial k} \Delta k + \frac{\partial \ln I}{\partial w} \Delta w. \quad (8)$$

In the form of the logarithm of normalized radiances, PA is physically related to the optical depth change $\Delta \tau$. Figure 3 compares the partial derivatives of radiances to slit parameters in HR and ER simulations. Little difference is found even though convolution error for ozone cross sections is only accounted for in the ER simulation due to the overwhelming impact of ozone cross section convolution errors over other cross section data.

Furthermore, this linearization process can be formulated with n-order polynomial fitting parameters (Δp_i) to account for the wavelength-dependent change of the slit parameters around a central wavelength $\bar{\lambda}$ and consequently, the total PA is expressed as

$$PA = \frac{\partial \ln I}{\partial k} \sum_{i=1}^n \Delta k_i \cdot (\lambda - \bar{\lambda})^{n-1} + \frac{\partial \ln I}{\partial w} \sum_{i=1}^n \Delta w_i \cdot (\lambda - \bar{\lambda})^{n-1}. \quad (9)$$

205

206 3. Results and Discussion

We characterize the effect of including the PA ($\frac{\partial \ln I}{\partial p} \cdot \Delta p$) on ozone profile retrievals using both Super Gaussian and standard Gaussian slit functions. Hereafter, the correction spectrum ($\frac{\partial \ln I}{\partial p}$) is derived using the HR simulation. The PA coefficient (Δp_i) (one for each channel and for each order) is included as part of the state vector to be iteratively and simultaneously retrieved with ozone. The a priori value is set to be zero



211 for all fitting coefficients, while the a priori error is set to be 0.1, empirically. We should note that the
212 empirical “soft calibration” is applied to OMI radiances before the spectral fitting, in order to eliminate the
213 wavelength and cross-track dependent systematic biases, due to the interference of the PA coefficients with
214 systematic measurement errors during the fitting process.

215 **3.1 Characterization of the pseudo absorbers in ozone fitting procedure**

216 Figure 4 displays how the zero-order PA coefficients (Δp) vary within one orbit when slit functions are
217 assumed as standard and Super Gaussians, respectively, along with variation of cloud fraction, surface
218 albedo, and cloud pressure from the retrievals. These fitting coefficients physically represent the difference
219 of slit parameters between radiance and irradiance in this implementation. Therefore, we normalize them
220 with the slit parameters derived from OMI solar irradiances for a better interpretation. Cross-track
221 dependent features are shown in slit width. The relative change of the slit width is more distinct in the UV1
222 band than in the UV2 band, whereas the change of the shape factor is more distinct in the UV2 band. The
223 UV2 slit widths increase typically within 5 % over the given spatial domain. However, the UV1 slit widths
224 increase from 10 % at most pixels up to 50 % at off-nadir positions in the high latitudes, which might be
225 caused by stray light differences between radiance and irradiance and intra-orbit instrumental changes. An
226 abnormal change of the UV1 slit parameters due to the scene heterogeneity is detected at the along-track
227 scan positions of ~ 300 and 900 , respectively, where upper-level clouds are present. The UV2 shape factor
228 changes show a coherent sensitivity to bright surfaces under clear-sky condition over the northern high
229 latitudes. Fitting coefficients for the standard Gaussian show a quite similar spatial variation for the UV1
230 slit width (correlation = ~ 0.98), but an anti-correlation of ~ -0.62 for the UV2 slit width compared to those
231 for Super Gaussian due to the interference between shape factor and slit width.

232 Examples of the total PAs (eq. 9) are illustrated in Figure 5 when (a) zero and (b) first-order polynomial
233 are fitted, respectively. The UV1 total PA spectrum, regardless of which Gaussian is assumed as slit
234 function, is very similar because the spectral structure caused by the slit width change is dominant. It implies
235 that OMI ISRFs in the UV1 band are similar to the standard Gaussian, for both radiance and irradiance
236 measurements, consistent with the pre-launch characterization (Dirksen et al., 2006). However, in the UV2
237 band, the PA is mostly contributed from the shape factor change in the case of super Gaussian, and the total
238 PA spectrum is more noticeable for super Gaussian. Our results indicate that the PA for the shape factor
239 change is required to adjust the spectral structures due to the differences in the slit functions between
240 radiance and irradiance over the UV2 band. In the case of the wavelength dependent ISRF fit, the impact
241 of first-order PAs on OMI radiances is relatively visible in the wavelength range of 300-310 nm. This result
242 is physically consistent with the wavelength dependent property shown in the slit parameters derived from
243 OMI irradiances as shown in Figure 6 where slit parameters are characterized in 10-pixel increments



244 assuming the super Gaussian slit function. In UV1, the slit widths plotted as FWHM slightly decrease by ~
245 0.1 nm at shorter wavelengths than 288 nm, but more sharply vary by up to ~0.2 nm at longer wavelengths.
246 Compared to slit widths, the wavelength dependences of the shape factors are less noticeable, except at
247 boundaries of the window. In the UV2 window, both slit width and shape factor are highly invariant.

248 **3.2 Impact of including pseudo absorbers on ozone profile retrievals**

249 Figures 7 to 10 evaluate the impact of including zero-order PAs on ozone profile retrievals. Figure 7
250 illustrates how different assumptions in the slit functions affect the ozone profile retrievals with respect to
251 the retrieval sensitivity and the fitting accuracy from the case shown in Figure 4. In this figure, the Degrees
252 of Freedom for Signal (DFS) represents the independent pieces of ozone information available from
253 measurements, which typically decreases as ozone retrievals are further constrained by other fitting
254 variables. The reduced DFS values (< 5 %) imply that the ozone retrievals are correlated slightly with PAs.
255 The fitting accuracy is assessed as the root mean square (RMS) of relative difference (%) between measured
256 and calculated radiances over the UV1 and UV2 ranges, respectively. Including the PAs makes little
257 difference in the UV1 fitting residuals for most of individual pixels (1-5 %), but significantly reduces
258 residuals in the UV2 range. The adjusted amount of the residuals with PAs are generally larger when
259 assuming super Gaussian slit functions. This comes from different assumptions for slit functions in deriving
260 soft calibration spectra, where slit functions were parameterized as standard Gaussians. Therefore, applying
261 soft calibration to OMI spectra entails somewhat artificial spectral structures if ISRFs are assumed as Super
262 Gaussian in ozone retrievals, and hence the impact of PAs on the spectral fitting becomes more considerable.
263 Figure 8 compares how the spectral residuals are adjusted with PAs when soft calibration is turned on and
264 off, respectively. Using super Gaussians causes larger amplitudes of the spectral fitting residuals than using
265 standard Gaussians, if soft calibration is turned on and PAs are excluded. On the other hand, some residuals
266 are reduced and more broadly structured if soft calibration is turned off. Including PAs eliminates/reduces
267 some spikes of fitting residuals as well as improves the consistency of the fitting accuracy between using
268 standard and super Gaussians at wavelengths above 300 nm.

269 The benefit of this implementation on ozone retrievals is further assessed through comparison with
270 Electrochemical Concentration Cell (ECC) ozonesondes collected from the WOUDC (<https://woudc.org/>)
271 and SHADOZ (<https://tropo.gsfc.nasa.gov/shadoz/>) networks during the period 2005 to 2008. We select 13
272 SHADOZ sites in the tropics and 38 WOUDC sites in the northern mid/high latitudes. The collocation
273 criteria is within +/- 1 ° in latitude and longitude and within 12 hours in time. For comparison, high-vertical
274 resolution (~100 nm) profiles of ozonesondes are interpolated onto OMI retrieval grids (~2.5 km thick).
275 We limit OMI/ozonesonde comparisons to OMI solar zenith angle < 85°, effective cloud fraction < 0.4,
276 surface albedo < 20 % (100 %) in tropics and mid-latitudes (high latitude), top altitude of ozonesondes >



277 30 km, ozonesonde correction factors ranging from 0.85 to 1.15 if they exist, and data gaps for each
278 ozonesonde no greater than 3km. Comparisons between OMI and ozonesondes are performed for the
279 tropospheric ozone columns (TCOs) over 3 different latitude bands and for ozone profiles including all the
280 sites, with and without PAs (zero-order) for standard and super Gaussian slit function changes, respectively.

281 Figure 9 shows the comparisons of tropospheric ozone columns as scatter plots. Without using PAs, the
282 retrievals show significant differences of (1.2-2.2 DU or 3.8-6.4%) especially in mean biases between super
283 and standard Gaussians, with negative biases of 0.2-0.7 DU for super Gaussians and positive biases of 0.8-
284 1.5 DU for standard Gaussians. Overall, OMI retrievals are in a better agreement with ozonesonde
285 measurements using super Gaussians. The correlations and standard deviations are very similar in the
286 tropics and mid-latitudes, but the retrievals with standard Gaussians show better correlation and smaller
287 standard deviations in high-latitudes. Consistent with Sun et al (2017), the retrievals show significant
288 differences between using standard and super Gaussians, although there are some inconsistencies in
289 comparing OMI and ozonesondes; the main inconsistent factors are listed as following: In this study, soft
290 calibration is turned on and a priori information is taken from TB climatology to perform OMI ozone profile
291 retrievals, whereas soft calibration is turned off and a priori information is taken from LLM climatology in
292 Sun et al. (2017). OMI/ozonesonde data filtering criteria are quite similar to each other, except that the
293 criteria of the solar zenith angle and cloud fraction are relaxed from 75° and 0.3 to 85° and 0.4, respectively,
294 and the adjustment of ozonesondes with correction factor given for the WOUDC dataset is turned on in this
295 study. Comparison is performed by latitudes here whereas global comparison is analyzed in Sun et al.
296 (2017). After accounting for the slit differences between radiances and irradiances using PAs, the retrievals
297 are significantly improved for both standard and super Gaussians and these two retrievals become consistent
298 except for the use of super Gaussians in the tropics. The mean biases in the tropics and mid-latitudes are
299 almost eliminated, to within 0.3 DU, but the standard deviations and correlation do not change much,
300 slightly worse in the tropics and better in the mid-latitudes. In the high-latitudes, the standard deviations
301 and correlation are significantly improved especially for using super Gaussians, but the mean biases are
302 similar to the standard Gaussian without PAs. The lack of improvement with PAs in the tropics with super
303 Gaussians illustrates that ISRFs of radiances are quite similar to those of irradiances in the tropics, while
304 super Gaussians better parameterize OMI ISRFs than standard Gaussians. This is consistent with the
305 comparison of the fitting accuracy of the UV2 band as shown in Figure 7, where the fitting residuals are
306 slightly reduced in the tropics when super Gaussians are linearized, but the standard Gaussian linearization
307 significantly improves the fitting accuracy. The mean biases of the profile comparison as shown in Figure
308 10 clearly shows that including PAs to account for ISRF differences significantly reduces mean biases
309 below 10 km and the general altitude dependence and improves the consistency between using standard
310 and super Gaussians; the standard deviations also show noticeable improvement in the altitude range of 10-



311 20 km for both Gaussians. The significant improvement at all latitudes corroborates the change of ISRFs
312 between radiance and irradiance along the orbit as conjectured by Sun et al. (2017). The consistency
313 between using standard and super Gaussians after using PAs is mainly because there is strong anti-
314 correlation between the slit width and shape partial derivatives as shown in Figure 2, so the adjustment of
315 slit width only in the use of standard Gaussian can achieve almost the same effect as the adjustment of both
316 parameters in the use of super Gaussian. Accounting for the wavelength dependent change of the ISRFs
317 with first-order PAs makes insignificant differences to both fit residuals and ozone retrievals (not shown
318 here). This could be mainly explained with the fact of the negligible wavelength dependence of OMI ISRFs
319 especially in UV2 as shown in Figure 5 where the PA spectrum ($\frac{\partial \ln I}{\partial p} \cdot \Delta p$) shows almost no variance,
320 except at the upper boundary of the UV1 as well as in Figure 6 where the UV2 slit parameters derived from
321 irradiances in the sub-fit windows vary within 0.05 nm for FWHM and 0.2 for shape factor.

322

323 4. Summary

324 The knowledge of the Instrument Spectral Response Functions (ISRFs) or slit functions is important
325 for ozone profile retrievals from the Hartley and Huggins bands. ISRFs can be measured in the laboratory
326 prior to launch, but they have been typically derived from solar irradiance measurements assuming
327 Gaussian-like functions in order to account for the effect of the ISRF changes after launch. However, the
328 parameterization of the ISRFs from solar irradiances could be inadequate for achieving a high accuracy of
329 the fitting residuals as ISRFs in radiances could significantly deviate from those in solar radiances (Beirle
330 et al., 2017) and might affect ozone profile retrievals as suggested in Sun et al. (2017). Therefore, this study
331 implements a linearization scheme to account for the spectral errors caused by the ISRFs changes as Pseudo
332 Absorbers (PAs) in an optimal estimation based fitting procedure for retrieving ozone profiles from OMI
333 BUUV measurements using the SAO ozone profile algorithm. The ISRFs are assumed to be the generic super
334 Gaussian that can be used as standard Gaussian when fixing the shape factor to 2. This linearization was
335 originally introduced in Beirle et al. (2017) for DOAS analysis, but this study extends this application and
336 more detail how to implement in practice using two different approaches to derive radiance errors from slit
337 function partial derivatives with respect to slit parameters. These two approaches correspond to the two
338 methods of simulating radiances at instrument spectral resolution, one using effective cross sections which
339 were previously used in the SAO ozone profile algorithm and are still used in most of the trace gas retrievals
340 from the UV and visible, and the other calculating radiances at high resolution before convolution, which
341 is the preferred method in the SAO ozone profile algorithm. Consistent PAs are derived with these two
342 approaches, as expected.



343 The fitting coefficients (Δp) to the PAs, representing the difference of slit parameters between radiance
344 and irradiance, are iteratively fitted as part of the state vector along with ozone and other parameters. The
345 UV1 slit parameters show distinct cross-track-dependent differences, especially in high-latitudes. In
346 addition, an abnormal Δp caused by scene heterogeneity is observed around bright surfaces and cloudy
347 scenes. The total PA spectrum ($\frac{\partial I}{\partial p} \cdot \Delta p$) illustrates that the slit width change causes most of the spectral
348 structures in the UV1 band because the OMI ISRFs are close to Gaussian. Otherwise, the ISRF change
349 results into different spectral responses in the UV2 band with different Gaussian functions because the
350 adjustment of the shape factor becomes more important in accounting for the convolution error when using
351 super Gaussians.

352 Insignificant wavelength dependence on OMI slit functions is demonstrated from slit function
353 parameters derived from irradiances in the sub-fit window, which leads to little difference in ozone profile
354 retrievals when zero and first-order wavelength dependent PA coefficients are implemented to fit the
355 spectral structures caused by slit function errors, respectively. Therefore we evaluate the benefit of
356 including the zero-order PAs fit on both the accuracy of the fitting residuals and the quality of retrieved
357 ozone profiles through validation against ozonesonde observations. Some spikes in the fitting residuals are
358 reduced or eliminated. Commonly, including PAs makes little change on both fit residuals and ozone
359 retrievals in the tropics if a super Gaussians are assumed as ISRFs but this is not the case for the standard
360 Gaussian assumption. Retrievals using standard and super Gaussians agree better if slit function errors are
361 accounted for by including PAs. Using PAs ultimately demonstrates substantial improvement of ozone
362 profile retrievals in the comparison of tropospheric ozone columns and ozone profiles up to 30 km. Using
363 super Gaussians, the TCO comparison shows significant improvement in mean biases in mid-latitudes and
364 in standard deviations in high-latitudes. Using standard Gaussians, the TCO comparison also shows
365 significant improvement in mean biases in the tropics. The profile comparison generally shows
366 improvement in mean biases as well as in standard deviation in the altitude range 10-20 km. More
367 importantly, using these PAs make the retrieval consistent between standard and super Gaussians. Such
368 consistency is due to the anti-correlation between slit width and shape PAs. This study demonstrates the
369 slit function differences between radiance and irradiance and its usefulness to account for such differences
370 on the pixel-to-pixel basis. In this experiment, the soft spectrum, derived with the standard Gaussian
371 assumption, is applied to remove systematic measurement errors before spectral fitting, indicating that the
372 evaluation of ozone retrievals might be unfairly performed for the super Gaussian function implementation.
373 Nonetheless, OMI ozone profile retrievals show better agreement with ozonesonde observations when the
374 super Gaussian is linearized. Actually, the fitting residuals are slightly more broadly structured with super
375 Gaussians than with standard Gaussians if the soft-calibration and PAs are turned off, indicating the benefit



376 of deriving a soft calibration with the super Gaussians. Therefore, there is still room for achieving better
377 benefits when using the PAs on ozone profile retrievals by applying the soft calibration derived with super
378 Gaussians.

379

380 **Acknowledgement**

381 We acknowledge the OMI science team for providing their satellite data and the WOUDC and SHADOZ
382 networks for their ozonesonde datasets. Research at the Smithsonian Astrophysical Observatory by J. Bak,
383 X. Liu, K. Sun, and K. Chance was funded by NASA Aura science team program (NNX14AF16G &
384 NNX17AI82G).

385

386 Azam, F. and Richter, A.: GOME2 on MetOp: Follow on analysis of GOME2 in orbit degradation, Final
387 report, EUM/CO/09/460000696/RM, 2015, available at: [http://www.doas](http://www.doas.bremen.de/reports/gome2_degradation_follow_up_final_report.pdf)
388 [bremen.de/reports/gome2_degradation_follow_up_final_report.pdf](http://www.doas.bremen.de/reports/gome2_degradation_follow_up_final_report.pdf) (last access: 7 September 2016),
389 2015.

390 Bak, J., Liu, X., Wei, J. C., Pan, L. L., Chance, K., and Kim, J. H.: Improvement of OMI ozone profile
391 retrievals in the upper troposphere and lower stratosphere by the use of a tropopause-based ozone profile
392 climatology, Atmos. Meas. Tech., 6, 2239–2254, doi:10.5194/amt-6-2239-2013, 2013.

393 Bak, J., Liu, X., Kim, J.-H., Haffner, D. P., Chance, K., Yang, K., and Sun, K.: Characterization and
394 correction of OMPS nadir mapper measurements for ozone profile retrievals, Atmos. Meas. Tech., 10,
395 4373–4388, <https://doi.org/10.5194/amt-10-4373-2017>, 2017.

396 Beirle, S., Sihler, H., and Wagner, T.: Linearisation of the effects of spectral shift and stretch in DOAS
397 analysis, Atmos. Meas. Tech., 6, 661–675, doi:10.5194/amt-6-661-2013, 2013.

398 Beirle, S., Lampel, J., Lerot, C., Sihler, H., and Wagner, T.: Parameterizing the instrumental spectral
399 response function and its changes by a super-Gaussian and its derivatives, Atmos. Meas. Tech., 10, 581–
400 598, <https://doi.org/10.5194/amt-10-581-2017>, 2017.

401 Brion, J., Chakir, A., D. Daumont, D., and Malicet, J.: High-resolution laboratory absorption cross section
402 of O₃. Temperature effect, Chem. Phys. Lett., 213(5–6), 610–612, 1993.

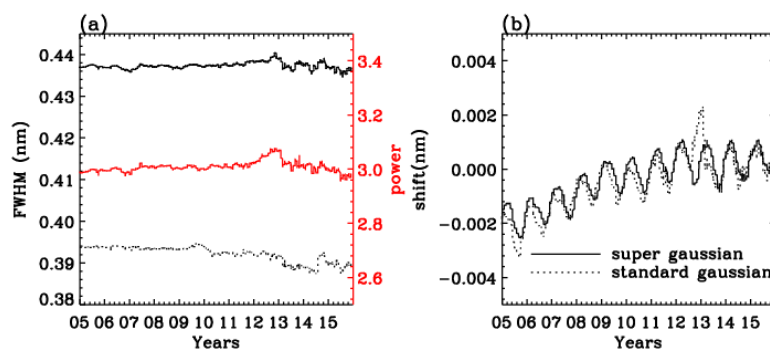
403 Cai, Z., Liu, Y., Liu, X., Chance, K., Nowlan, C. R., Lang, R., Munro, R., and Suleiman, R.: ,
404 Characterization and correction of Global Ozone Monitoring Experiment 2 ultraviolet measurements
405 and application to ozone profile retrievals, J. Geophys. Res., 117, D07305, doi:10.1029/2011JD017096,
406 2012.

407 Caspar, C. and Chance, K.: GOME wavelength calibration using solar and atmospheric spectra, Third ERS
408 Symposium on Space at the Service of our Environment, Florence, Italy, 14–21 March, 1997.

409 Dobber, M., Voors, R., Dirksen, R., Kleipool, Q., and Levelt, P.: The high-resolution solar reference
410 spectrum between 250 and 550 nm and its application to measurements with the Ozone Monitoring
411 Instrument, Solar Physics, 249, 281–291, 2008. Kim, P. S., Jacob, D. J., Liu, X., Warner, J. X., Yang,



- 412 K., Chance, K., Thouret, V., and Nedelec, P.: Global ozone–CO correlations from OMI and AIRS:
413 constraints on tropospheric ozone sources, *Atmos. Chem. Phys.*, 13, 9321–9335,
414 <https://doi.org/10.5194/acp-13-9321-2013>, 2013.
- 415 Kim, P. S., Jacob, D. J., Liu, X., Warner, J. X., Yang, K., Chance, K., Thouret, V., and Nedelec, P.: Global
416 ozone–CO correlations from OMI and AIRS: constraints on tropospheric ozone sources, *Atmos. Chem.*
417 *Phys.*, 13, 9321–9335, <https://doi.org/10.5194/acp-13-9321-2013>, 2013.
- 418 Levelt, P. F., van den Oord, G. H. J., Dobber, M. R., Malkki, A., Visser, H., de Vries, J., Stammes, P.,
419 Lundell, J. O. V., and Saari, H.: The ozone monitoring instrument, *IEEE Transactions on Geoscience*
420 *and Remote Sensing*, 44, 1093–1101, doi:10.1109/TGRS.2006.872333, 2006.
- 421 Liu, X., Chance, K., Sioris, C. E., Spurr, R. J. D., Kurosu, T. P., Martin, R. V., and Newchurch, M. J.:
422 Ozone profile and tropospheric ozone retrievals from Global Ozone Monitoring Experiment: algorithm
423 description and validation, *J. Geophys. Res.*, 110, D20307, doi: 10.1029/2005JD006240, 2005.
- 424 Liu, X., Bhartia, P.K, Chance, K, Spurr, R.J.D., and Kurosu, T.P.: Ozone profile retrievals from the ozone
425 monitoring instrument. *Atmos. Chem. Phys.*, 10, 2521–2537, 2010.
- 426 Liu, C., Liu, X., Kowalewski, M.G., Janz, S.J., González Abad, G., Pickering, K.E., Chance, K., and
427 Lamsal, L.N.: Characterization and verification of ACAM slit functions for trace gas retrievals during
428 the 2011 DISCOVER-AQ flight campaign, *Atmos. Meas. Tech.*, 8, 751–759, doi:10.5194/amt-8-751-
429 2015, 2015.
- 430 Sioris, C. E. and Evans, W. F. J.: Impact of rotational Raman scattering in the O₂ A band, *Geophys. Res.*
431 *Lett.*, 27, 4085–4088, 2000.
- 432 Spurr, R. J. D.: Linearized pseudo-spherical scalar and vector discrete ordinate radiative transfer models
433 for use in remote sensing retrieval problems, in: *Light Scattering Reviews*, edited by: Kokhanovsky, A.,
434 Springer, New York, 2008.
- 435 Sun, K., Liu, X., Huang, G., González Abad, G., Cai, Z., Chance, K., and Yang, K.: Deriving the slit
436 functions from OMI solar observations and its implications for ozone-profile retrieval, *Atmos. Meas.*
437 *Tech.*, 10, 3677–3695, <https://doi.org/10.5194/amt-10-3677-2017>, 2017.
- 438 van Hees, R. M., Tol, P. J. J., Cadot, S., Krijger, M., Persijn, S. T., van Kempen, T. A., Snel, R., Aben, I.,
439 and Hoogeveen, Ruud W. M.: Determination of the TROPOMI-SWIR instrument spectral response
440 function, *Atmos. Meas. Tech.*, 11, 3917–3933, <https://doi.org/10.5194/amt-11-3917-2018>, 2018.
- 441 Wilmouth, D. M., Hanisco, T. F., Donahue, N. M., and Anderson, J. G.: Fourier transform ultraviolet
442 spectroscopy of the A₂Π_{3/2} – X²Π_{3/2} Transition of BrO, *J. Phys. Chem. A.*, 103(45), 8935–8945, 1999.
- 443
- 444
- 445
- 446
- 447
- 448



449

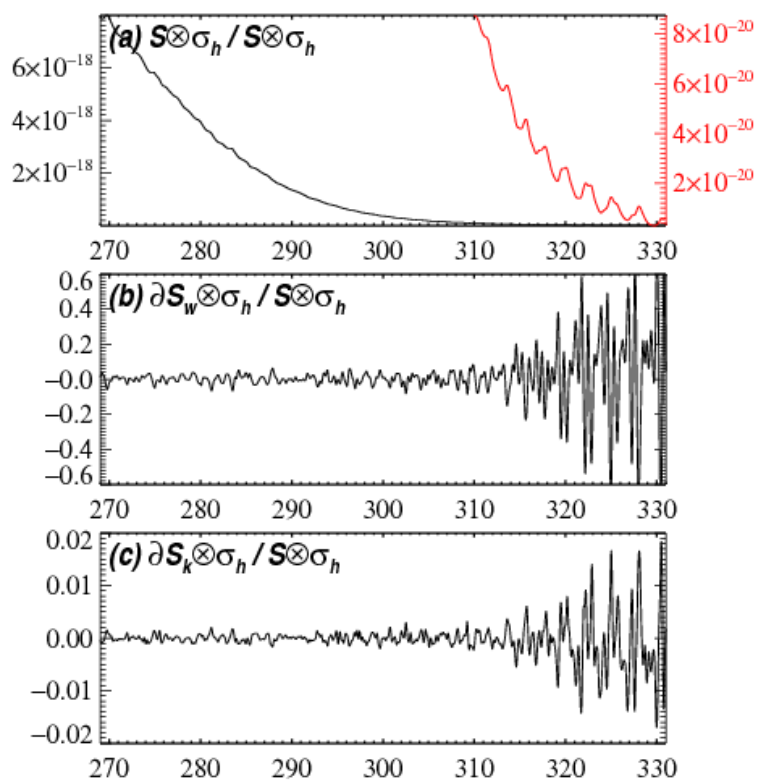
450 **Figure 1. Time series of (a) slit parameters and (b) wavelength shifts for OMI daily irradiance**
451 **measurements (310-330 nm) at nadir cross track position when Super Gaussians (solid line) and**
452 **standard Gaussians (dotted line) are parameterized as slit function shapes, respectively.**

453

454

455

456

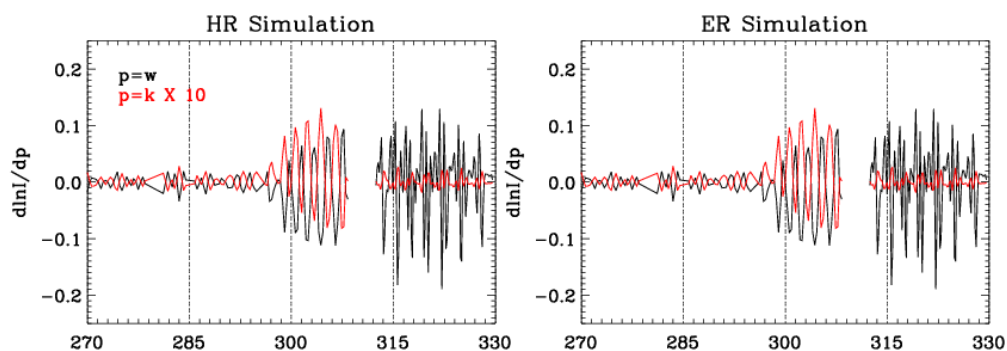


457

458 **Figure 2. (a) Ozone absorption cross sections ($\text{cm}^2/\text{molecule}$) (δ_h) at different scales (red and black) at**
 459 **a representative temperature (238.12 K) calculated via convolution of high-resolution (0.01 nm)**
 460 **reference spectrum with the Super Gaussian slit function, S ($k = 2.6, w = 0.26 \text{ nm}$)). (b) and (c) its**
 461 **derivatives with respect to slit parameters ($\partial S_p = \frac{\partial S}{\partial p}$), w and k , respectively, normalized to the**
 462 **convolved cross sections.**

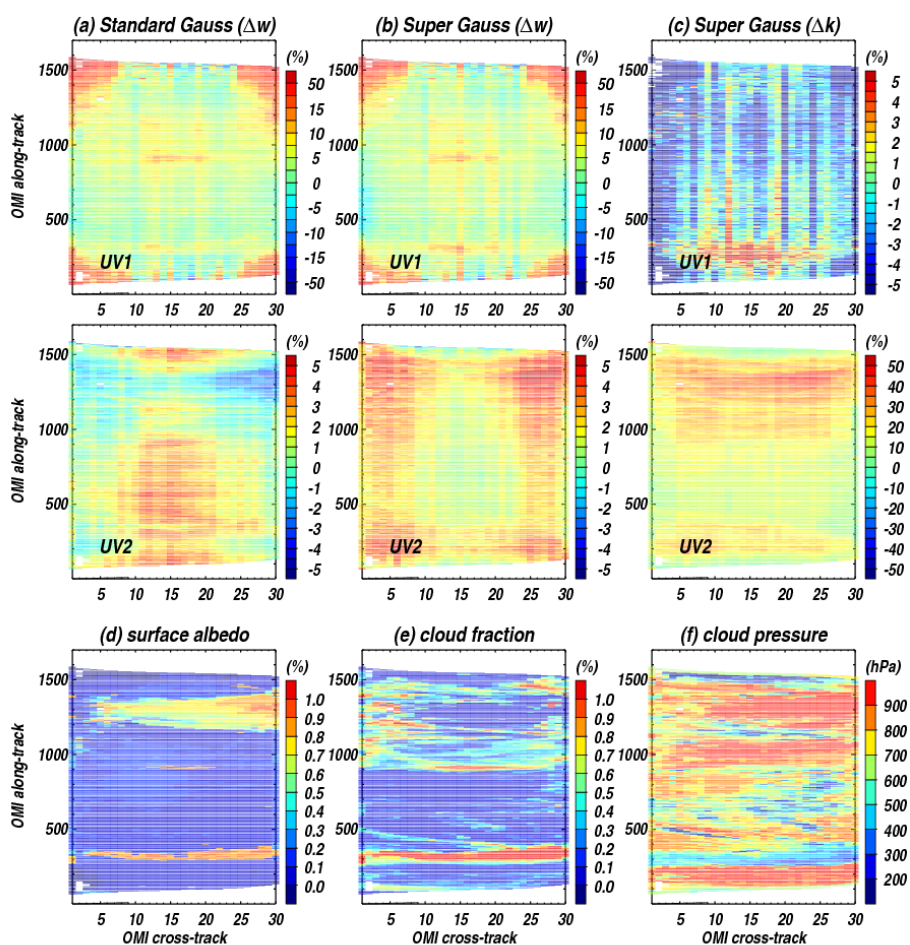
463

464



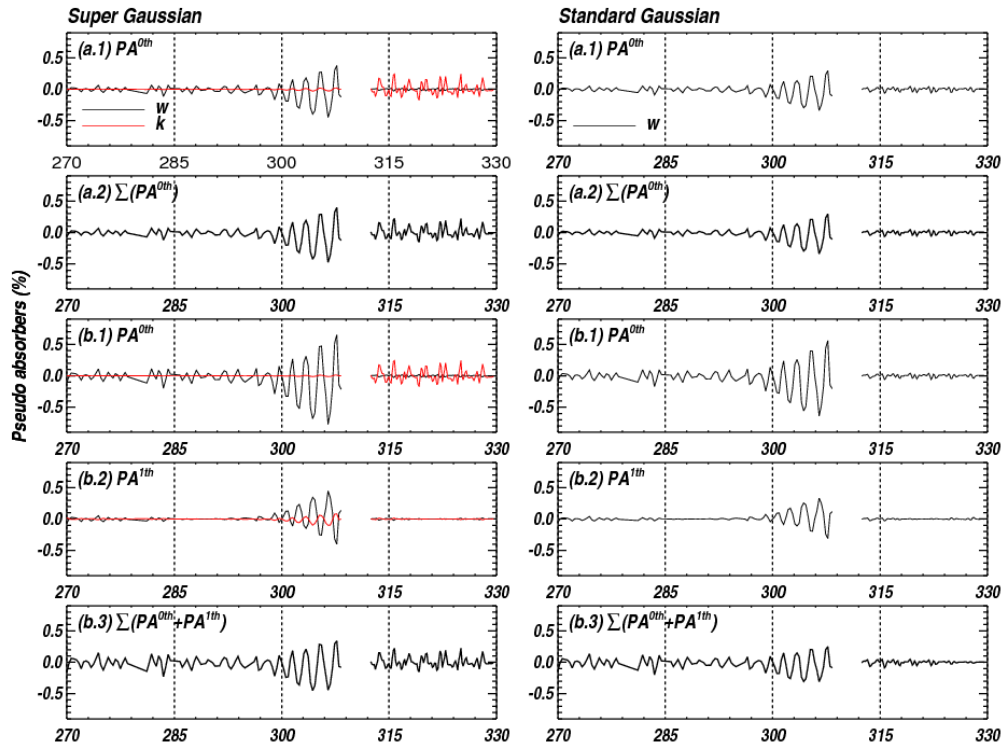
465

466 **Figure 3. Derivatives of OMI radiance spectrum simulated using high-resolution (HR) and effective**
467 **resolution (ER) cross section spectra with respect to slit parameters assuming a Super Gaussian function.**
468 **$d\ln I/dk$ is multiplied by a factor of 10 to visually match $d\ln I/dw$ in the same y-axis.**



469

470 **Figure 4.** Pseudo absorption coefficients ($\Delta w, \Delta k$) for fitting the OMI radiances due to slit function
 471 changes assuming (a) standard Gaussian and (b-c) Super Gaussian, within the first orbit of
 472 measurements on 1 July 2006, with (d-f) the corresponding geophysical parameters. Δw and Δk is
 473 displayed after being normalized with w_o , and k_o , the slit parameters derived from OMI solar
 474 irradiance measurements.



475

476

477

478

479

480

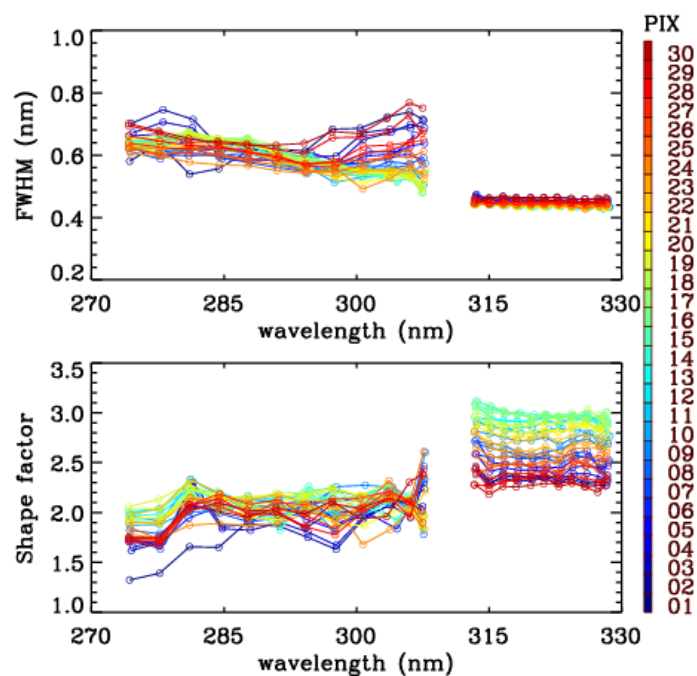
481

482

483

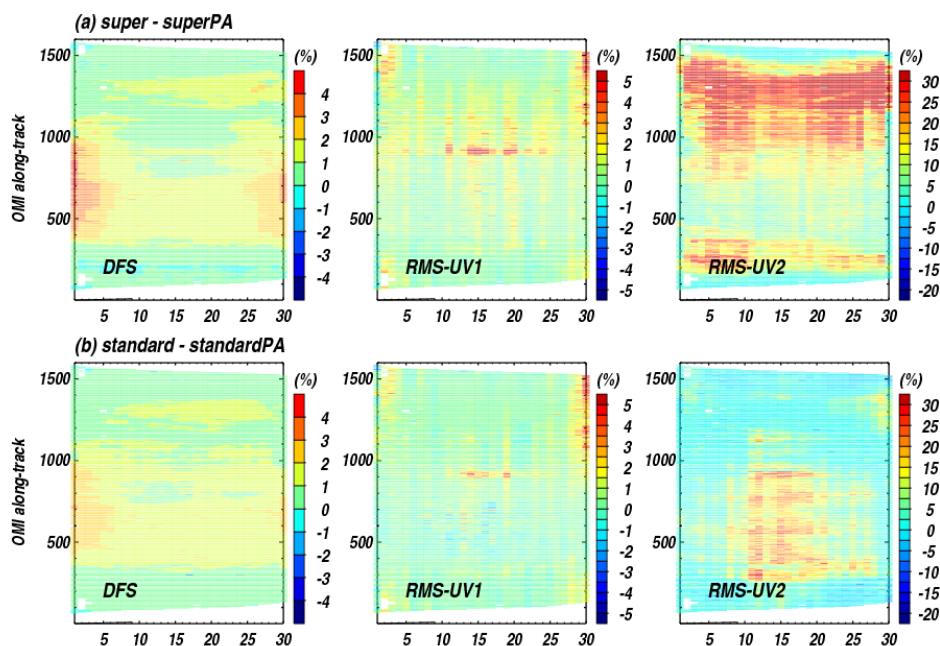
484

Figure 5. (a.1) Pseudo absorber spectra ($\frac{\partial \ln I}{\partial p} \times \Delta p$) for zero order slit parameters and (a.2) its total spectra for (left) Super Gaussian and (right) Standard Gaussian function parameterizations, respectively. (b) Same as (a), but for first order polynomial fit. The case represents an average at nadir in the latitude zone 30°-60°N.



485

486 **Figure 6.** OMI ISRF FWHM (nm) and shape factor (k) as functions of the center wavelength, as derived
487 from OMI solar irradiances assuming Super Gaussian functions over a range of 31 spectral pixels in 10-
488 pixel increments. Different colors represent different cross-track positions from 1 (blue) to 30 (red).



489

490 **Figure 7.** Same as Figure 4, but for comparisons of the Degrees of Freedom for Signal (DFS) and the Root
 491 **Mean Square (RMS) of spectra fitting residuals in UV 1 and UV2 with and without zero-order pseudo**
 492 **absorber. Positive values indicate that both fitting residuals and DFSs are reduced due to the pseudo**
 493 **absorber.**

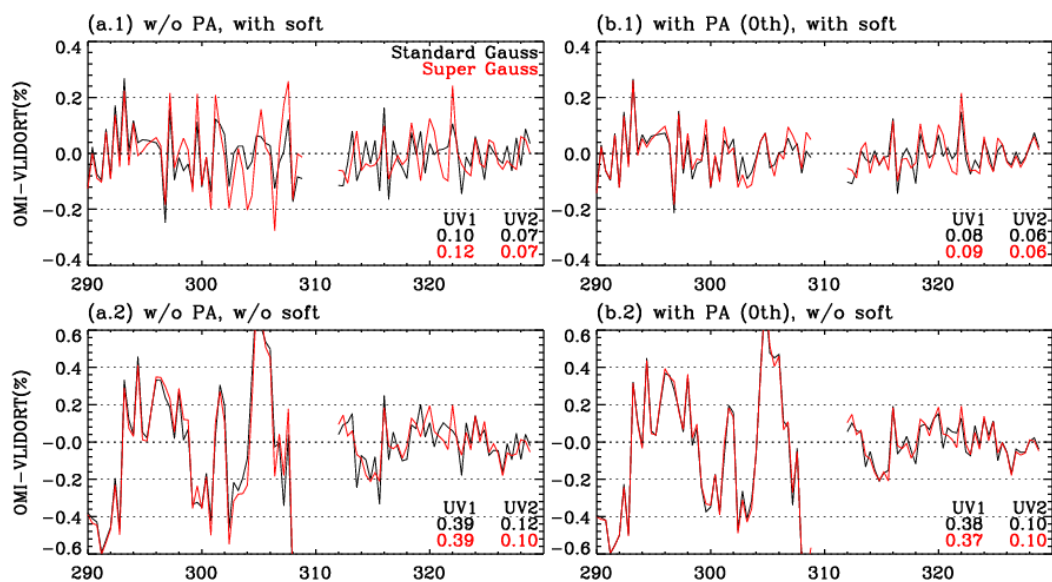
494

495

496

497

498



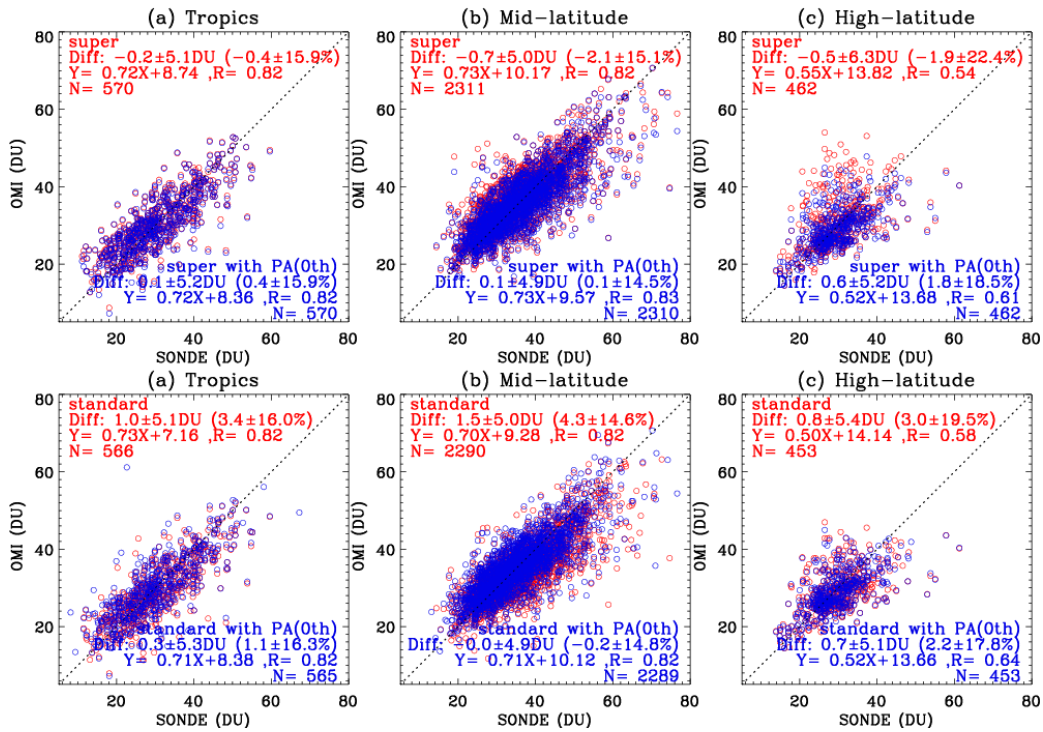
499

500 **Figure 8.** Average differences (%) between measured (OMI) and simulated (VLIDORT) radiances
 501 (residuals) at the nadir cross-track pixel in the tropics (30°S-30°S) without (a) and with (b) zero-order
 502 pseudo absorbers (PA) when the standard Gaussian (black line) and the Super Gaussian (red line) are
 503 assumed as ISRFs, respectively. Upper/lower panels represent the fit results with soft calibration being
 504 turned on/off. The residuals in the UV1 (< 310 nm) are scaled by a factor of 2 to fit in the given y-axis.
 505 In the legend, the RMS of residuals (%) are given for UV1 and UV2 wavelength ranges, respectively.

506

507

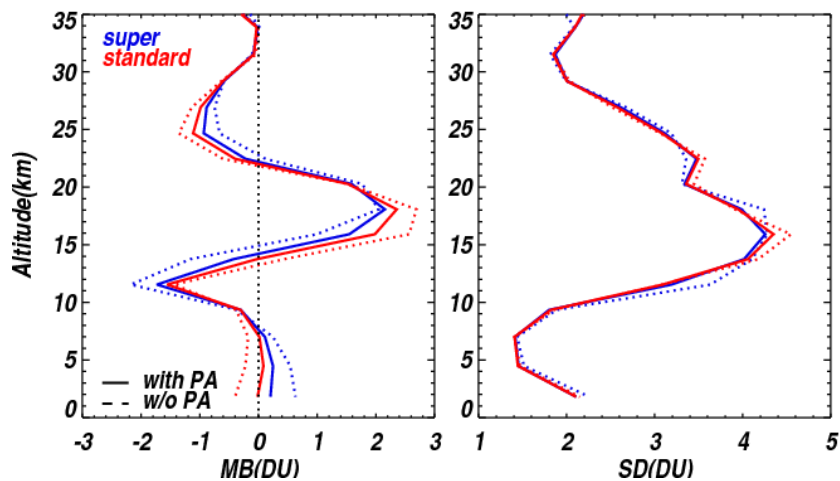
508



509

510 **Figure 9. Comparison of OMI and ozonesonde tropospheric column ozone over (a) the tropics (30°S-**
 511 **30°N), (b) mid-latitudes (30°N-60°N), (c) high-latitudes (60°N-90°N), with different slit function**
 512 **assumptions/implementations. Super and standard Gaussians are assumed as slit function for the upper**
 513 **and lower results, respectively. Different colors represent the implementations with (blue) and without**
 514 **(red) pseudo absorbers.**

515



516

517 **Figure 10. Global mean biases at each OMI layer and 1σ standard deviations of the differences between**
518 **OMI and ozonesondes, with different slit function assumptions/implementations.**

519

520

521

522